High resolution hematite and goethite records from ODP 1143, South China Sea: Co-evolution of monsoonal precipitation and El Niño over the past 600,000 years

Yi Ge Zhang [a,*], Junfeng Ji [a,1], William L. Balsam [b,2], Lianwen Liu [a,3], Jun Chen [a,4]

[a] *Institute of Surficial Geochemistry, Department of Earth Sciences, Nanjing University, Nanjing 210093, China*
[b] *Department of Earth and Environmental Sciences, University of Texas at Arlington, Arlington, TX 76019, USA*

Abstract

Precipitation has a larger variability than temperature in tropical monsoon regions, thus it is an important climate variable. However, reconstructions of long-term rainfall histories are scarce because of the lack of reliable proxies. Here we document that iron oxide minerals, specifically the ratio of hematite to goethite (Hm/Gt), is a reasonable precipitation proxy. Using diffuse reflectance spectrophotometry, we measured samples from Ocean Drilling Program (ODP) 1143 drilling site (9°21.72′N, 113°17.11′E, 2777 m water depth) for hematite and goethite, whose formation processes are favored by opposing climate conditions. In order to determine the content of hematite and goethite we produced a set of calibration samples by removing the iron oxides to generate the natural matrix to which hematite and goethite in known percentages were added. From these calibration samples we developed a transfer function for determining hematite and goethite concentration from a sample's spectral reflectance. Applying this method to ODP 1143 sediments (top 34 m of a 510 m core with sampling interval of 10 cm) we were able to reconstruct a continuous precipitation history for SE Asia of the past 600 kyr using the Hm/Gt ratio as a proxy of the precipitation variability of Asian monsoon. The reliability of this Hm/Gt proxy is corroborated by its consistency with the stalagmite $\delta^{18}O$ data from South China. Comparing long-term Hm/Gt records with the surface temperature gradient of equatorial Pacific Ocean, we found that monsoon precipitation and El Niño are correlated for the last 600 kyr. The development of El Niño-like conditions decreased SE Asia precipitation, whereas precipitation increases in response to La Niña intensification.
© 2007 Elsevier B.V. All rights reserved.

Keywords: Ocean Drilling Program; diffuse reflectance spectroscopy; hematite; goethite; Asian monsoon precipitation; El Niño

* Corresponding author. Present Address: Department of Marine Sciences, University of Georgia, Athens, GA 30602, USA. Tel.: +1 706 380 9188; fax: +1 706 542 5888.

E-mail addresses: ygzhang@uga.edu (Y.G. Zhang), jijunfeng@nju.edu.cn (J. Ji), balsam@uta.edu (W.L. Balsam), liulw@nju.edu.cn (L. Liu), chenjun@nju.edu.cn (J. Chen).

[1] Tel.: +86 25 83595795; fax: +86 25 83302728.
[2] Tel.: +1 817 272 2997; fax: +1 817 272 2628.
[3] Tel.: +86 25 83686042; fax: +86 25 83302728.
[4] Tel.: +86 25 83592941; fax: +86 25 83302728.

1. Introduction

Atmospheric precipitation is a key variable of climate. Over vast tropical and subtropical monsoon regions such as southern and southeastern Asia, monsoonal precipitation exerts greater impact on local ecosystem and human society than temperature. For example, annual rainfall in SE Asia often changes by more than 100% of its yearly mean value (Shen et al.,

2005). This highly variable precipitation factor largely controls the hydrological cycle (Webster, 1994), continental weathering/erosion in Southern and Southeastern Asia (Clift, 2006), and nutrient inputs to Indian and Pacific Ocean (Wei et al., 2003). The moisture bearing Asian monsoon, which originates in low latitudes and transports moisture and heat to higher latitudes, is important for climate change, because the variations in solar forcing that drives climate tend to be amplified in tropical regions (Yin and Battisti, 2001).

It is surprising that given the paramount importance of monsoonal precipitation, a clear, long-term, history of the variability of Asian monsoon precipitation has not been established. This is largely due to the lack of reliable proxy monitors of precipitation. Potential proxies include tree rings, mollusks, pollen, corals, charcoal, C3/C4 plants, and lake hydrological records (reviewed in Wang et al., 2005). Unfortunately, these proxies are either restricted to short a time span or are not tightly associated with the summer monsoon. One proxy, the $\delta^{18}O$ of speleothem calcite, preserves the oxygen isotopic composition of meteoric precipitation and can be precisely dated using the ^{230}Th method. As a result, recent studies of stalagmite calcite have provided significant insights into Asian monsoon history as far back as the penultimate glaciation (e.g. Cheng et al., 2006; Wang et al., 2001; Yuan et al., 2004). One of the most important findings of stalagmite studies is that intensity variations of the Asian summer monsoon generally followed Northern Hemisphere summer insolation, which is dominated by the precession period of Earth's orbit. Further, Asian monsoon circulation is not strongly affected by the glacial–interglacial climate cycles as previously assumed (Ruddiman, 2006). These results need additional verification by other types of records from regions affected by the Asian monsoon. Furthermore, new proxies are needed to reconstruct monsoon history longer than those permitted by U-series dating for coral and speleothems (~ 500 ka, Edwards et al., 1987).

We suggest that hematite (α-Fe$_2$O$_3$) and goethite (α-FeOOH), two iron oxide/oxyhydroxide minerals that commonly occur in soils and sediments, provides a reliable precipitation proxy. During silicate weathering, hematite and goethite formation are favored by opposite climate conditions (dry and warm for hematite, wet and cool for goethite) and their formation processes are competitive. Climatic factors govern the rate of formation and therefore the ratio of hematite to goethite (Kampf and Schwertmann, 1983; Schwertmann, 1988; Schwertmann and Murad, 1983). Thus, when the pedogenic hematite and goethite are recovered from sediments from the deep-sea (e.g. Harris and Mix, 1999, 2002) or loess deposits

(e.g. Balsam et al., 2004; Ji et al., 2004), their ratio may provide a record of precipitation changes.

However, it is difficult to determine the concentration of iron oxides in many sediments. Under optimal conditions the detection limit of X-ray diffraction (XRD) for hematite and goethite is ~ 1 wt.% (Deaton and Balsam, 1991). However, both minerals commonly occur at concentrations less than 1 wt.% in sediments. Mössbauer spectrometry only gives the relative proportion of Fe phases, and the analysis is time-consuming (Ji et al., 2002). Currently selective chemical extraction procedure still cannot separate hematite from goethite (Poulton and Canfield, 2005). Diffuse reflectance spectroscopy (DRS), on the other hand, is capable of detecting and quantifying Fe oxides in sediments with concentration as low as ~ 0.01 wt.% (Deaton and Balsam, 1991; Ji et al., 2002). Nonetheless, sample reflectance can be affected by other admixed minerals (the matrix effect); these effects need to be removed to determine hematite and goethite content (Deaton and Balsam, 1991; Ji et al., 2002). Ji et al. have shown that an effective method is to use the target sediments to prepare a set of calibration sample with known concentrations of hematite and goethite. These calibrations samples then serve as the basis for a transfer function for determining the concentration of hematite and goethite (Ji et al., 2002).

Here we apply this method to sediments from the Ocean Drilling Program (ODP) site 1143 (Fig. 1). The hematite and goethite in these samples formed in the soils of the Mekong basin and were transported by fluvial and marine processes to the site of ODP 1143 with little post-depositional modification. Using the hematite-to-goethite ratio (Hm/Gt) we produce a continuous record of monsoonal rainfall variations and provide details of long-term variability of Asian monsoon precipitation. In addition, we compare the results with the surface temperature gradient of equatorial Pacific, and show that monsoon precipitation and El Niño are strongly correlated for the last 600 kyr.

2. Materials

We used core samples recovered from ODP Site 1143 (9°21.72′N, 113°17.11′E, 2777 m water depth), southern South China Sea (SCS, Fig. 1). The SCS, one of the largest marginal basins along the west coast of Pacific, is sensitive to monsoon-induced climate change, to changes in detrital input from the continent, and to atmospheric and oceanic circulation (Wang et al., 2000). Site 1143 was drilled in a depression on the carbonate platform that forms the southern continental shelf of the SCS. It is located south of the Indochina upwelling
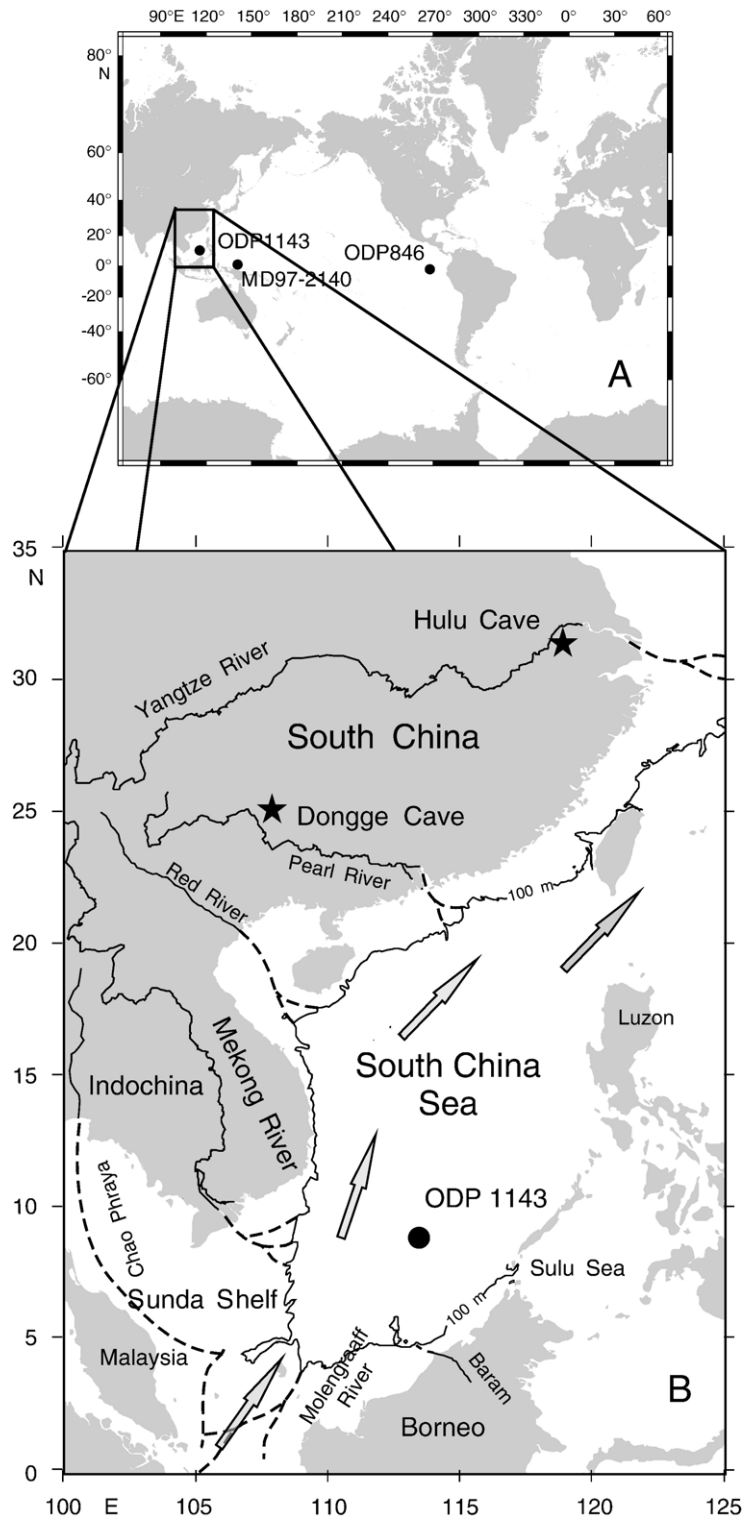
Fig. 1. Map shows (A) sites location of ODP 1143 (South China Sea, 9°21.72′N, 113°17.11′E, 2777 m water depth), IMAGES Site MD97-2140 (West Equatorial Pacific, 2°02′S, 141°46′E, 2547 m water depth) and ODP 846 (East Equatorial Pacific, 3°05′S, 90°49′W, 3296 m water depth; (B) the main monsoon regions of SE Asia, the location of ODP Site 1143 in South China Sea (black dot), the Mekong River, and Hulu/Dongge Cave in south China (stars). The thick line offshore corresponds to the present 100 m-isobath, approximating the lowest sea level during glacial maxima. Gray arrows indicate summer monsoon direction. After (Trentesaux et al., 2003).

region and close to the Mekong river estuary and the Sunda shelf (Fig. 1). The site is within the Western Pacific Warm Pool, a region of relatively high and stable sea surface temperature (Tamburini et al., 2003). Sediments from Hole 1143 consist of homogenous hemipelagic fine-grained terrigenous materials and biogenic nannofossil carbonate ooze. Terrigenous materials include primarily quartz, feldspar, clay minerals accounting for 99% or more of the clastic fraction. Minor biogenic components include sponge spicules and diatoms (average ∼2%, Wan et al., 2006). The Mekong River, whose sediment discharge is ∼160×10^6 t/year, and the Sunda Shelf contribute most of the terrigenous sediments deposited at site 1143 (Wan et al., 2006; Wang et al., 2000); eolian inputs are negligible (Liu et al., 2005; Wehausen et al., 2003). Soils in the Mekong basin (lower reach of the Mekong River, including Laos, Thailand, Cambodia and Vietnam) are likely the major contributor of hematite and goethite deposition at site 1143, because these secondary minerals are in low concentration in unweathered rocks or weakly-weathered soils which characterized the middle and upper reaches of Mekong (Liu et al., 2004).

Tian et al. (2002) established an astronomically calibrated timescale for ODP site 1143. They tuned changes of benthic foraminiferal oxygen isotopes to that of the Earth's orbit, with additional age constraints from magnetostratigraphic and biostratigraphic age determinations resulting in a high-resolution (∼2 kyr) chronology for the last 5 Ma (Tian et al., 2002). We calculated each sample's age using this chronologic framework. The upper 34 m of a 510 m core was sampled at an interval of 10 cm. The 315 samples used in our study span about the past 600 kyr; the time resolution between samples is ∼1.9 kyr.

3. Diffuse reflectance spectroscopy

The diffuse reflectance approach gives the percent reflectance of a sample at a certain wavelength relative to a white standard (reflectance%=100%). We used Spectralon™ as a standard. ODP 1143 cores were previously subject to spectral reflectance measurement onboard using a portable spectrophotometer, a Minolta CM-2002 (Wang et al., 2000). However, we find additional analysis necessary because (1) our shore-based spectrophotometer measures sample reflectance at a higher resolution, i.e. 2 nm vs. 10 nm onboard, which is critical for color band and first derivative value calculations. (2) Onboard measurements were taken on samples with varying water content which has an unpredictable influence on the reflectance data (Balsam et al., 1998). (3) Deep-sea

samples must be stored and oxidized so that DRS measurements can extract the greatest amount of information (Debret et al., 2006).

We analyzed the ODP 1143 samples using a diffuse reflectance spectrophotometer that is capable of measuring sample reflectance from near ultraviolet (190–400 nm), through the visible (400–700 nm) and into the near infrared (700–2500 nm). In this study we only used visible light because it is the wavelength range most sensitive to iron oxides (Deaton and Balsam, 1991). We analyzed all of the 315 samples using a Perkin-Elmer Lambda 900 spectrophotometer (Perkin-Elmer Corp., Norwalk, CT) with a diffuse reflectance attachment from 400 to 700 nm at 2 nm intervals. Sample preparation and analysis followed procedures described by Balsam and Deaton (1991). Ground samples were made into a slurry on a glass microslide with distilled water, smoothed, and dried slowly at low temperature (<40 °C, see Fig. 4 for microslide pictures). Reflectance data were processed to obtain percent reflectance in standard color bands (Judd and Wyszecki, 1975), i.e. violet=400–450 nm, blue=450–490 nm, green=490–560 nm, yellow=560–590 nm, orange=590–630 nm, red=630–700 nm (Fig. 2). These parameters served as independent variables in a transfer function for calculating hematite and goethite content (see below). Percent reflectance in the color bands was determined by dividing the percentage of reflectance in a color band by the total visible wavelength reflectance in a sample. Reflectance data were also used to compute the total reflectance of a sample or brightness (equivalent to L^* but calculated from the spectrum, Balsam et al., 1999) by summing a sample's reflectance values from 400–700 nm (Fig. 2). Replicate sample measurements ($n=5$) indicate that the precision of reflectance at a certain wavelength is better than +/−0.12%. When calculated for color bands or brightness, the precision is +/−0.08% on average. Data accuracy was controlled by frequent check of the Spectralon standard, with average standard deviation less than 0.1% at all wavelengths.

Previously, downcore measurements of brightness in ODP 1143 have been proposed as a proxy for carbonate content (Wang et al., 2000) since more light-colored carbonate increases the reflectance (Balsam et al., 1999). Brightness and therefore carbonate exhibit glacial–interglacial fluctuations superimposed on the ∼500 kyr long-term carbonate dissolution cycle (Bassinot et al., 1994a). Sample brightness continuously decreased from ∼500 ka as a result of the global carbonate dissolution cycle (Bassinot et al., 1994a). Thus we detrended the brightness record to ameliorate this long-term trend effect. The resulting time series of the brightness signal shows a
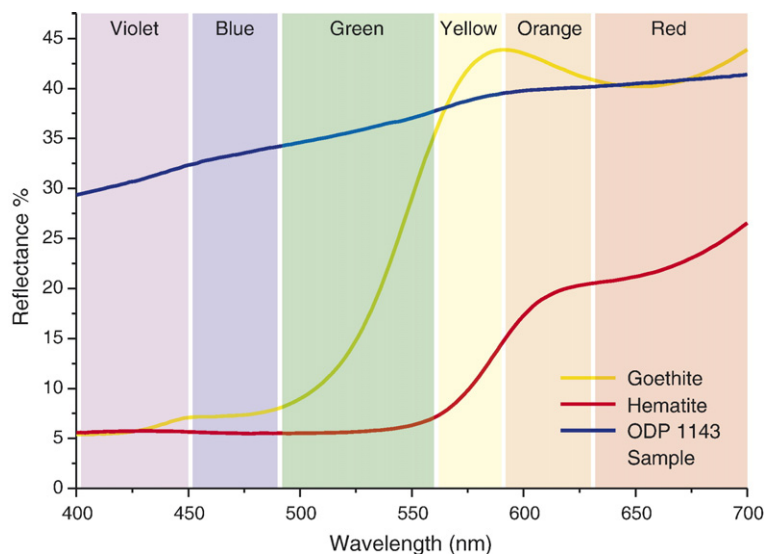
Fig. 2. Diffuse reflectance spectrum in the visible wavelength of the synthetic goethite and hematite used in this study, and a typical ODP Site 1143 sample (184/1143A/2H/5/15-16, 9.47 mcd). Reflectance data were processed to obtain percent reflectance in standard color bands (Judd and Wyszecki, 1975). The fall-off of sediment reflectance was primarily attributed to the absorption of iron oxides (Clark and Roush, 1984; Hunt and Salisbury, 1970). (For interpretation of the references to color in this figure legend, the reader is referred to the web version of this article.)

significant resemblance to benthic oxygen isotope records from the same core (Fig. 2, Tian et al., 2002). The carbonate cycles that govern 1143 sediments on orbital time scale may explain the correlation between brightness and the benthic $\delta^{18}O$. Two types of carbonate cycle exist in SCS: the "Pacific-type" carbonate cycles are only observed in sediments deposited at water depths below 3500 m, with higher carbonate content during glaciation. The classic "Atlantic-type" carbonate cycles are found at water depths above 3000 m. The ODP 1143 site, with a water depth of 2777 m falls into the Atlantic-type carbonate regime, showing lower carbonate content during glacials due to dilution by terrigenous detritus and higher carbonate content during interglacials (Wang et al., 1995). Thus, glacial samples of ODP 1143 are generally darker whereas interglacial samples are usually lighter, corresponding to the glacial cycles and therefore the $\delta^{18}O$ record.

4. Transfer functions for hematite and goethite measurement

When present, hematite and goethite account for much of the fall-off of sample reflectance, especially from 400 nm to 600 nm (Fig. 3, Clark and Roush, 1984; Hunt and Salisbury, 1970). Changes in the slope of the reflectance curve, that is the first-order derivative of the reflectance curve, more clearly demonstrate these changes. Peaks in first derivative curves have been used to indicate the presence of a variety of minerals,

especially iron oxides (Deaton and Balsam, 1991). Fig. 4A shows the result of a typical sample (184/1143A/3H/2/125–126, 16.25 mcd). Its first derivatives curve (Fig. 4A (b)) contains peaks around 445, 530 nm and 565 nm, in agreement with the goethite and hematite peak, respectively (Deaton and Balsam, 1991).

Although hematite and goethite in the samples can be easily detected from their reflectance, calculating their concentrations from the reflectance data is not straight-forward because both the color bands and first derivatives can be affected by minerals other than iron oxides; this is the so called matrix effect. Ji et al. (2002) measured hematite/goethite concentration in Chinese loess samples by calibrating them against a set of standard samples, prepared by adding hematite and goethite in known percentages. Using linear regression, they derived a transfer function for determining hematite and goethite content. We adopted this methodology to derive a function specifically for ODP 1143 sediments.

The reliability of this approach depends on the how closely the calibration samples resemble the natural samples. With this in mind we designed the following procedures (Fig. 4).

(1) Choosing samples. We chose 14 ODP 1143 samples from different depths to include diverse matrices. On microslides the prepared samples are brownish, and first derivatives reveal that they contain both hematite and goethite (Fig. 4A).
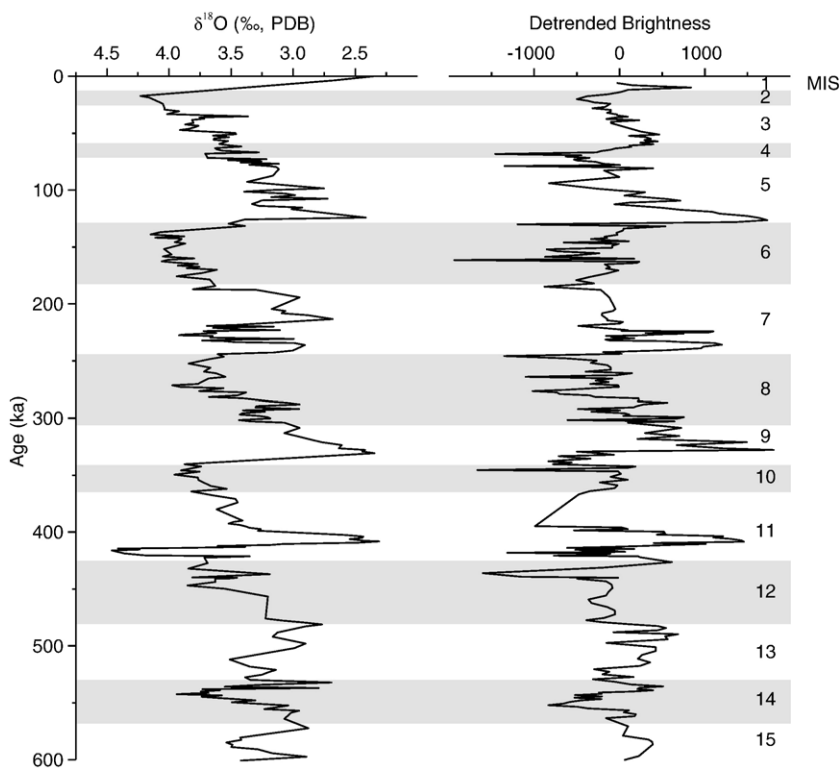
Fig. 3. Time series of benthic foraminiferal $\delta^{18}O$ curves and the brightness records of samples from ODP Site 1143. Left: Benthic $\delta^{18}O$ is based on *Cibicidoides wuellerstorfi*. (Tian et al., 2002). Right: Detrended brightness. The raw brightness data were subtracted by its 50-point FFT smoothing data to diminish the long-term trend derived from the carbonate dissolution cycle (∼ 500 kry, Bassinot et al., 1994a). Gray bars indicate glacial stages and numbers denote marine isotope stages (MIS).

(2) Deferrating samples. Each sample was treated with the CBD (citrate–bicarbonate–dithionite) procedure (Mehra and Jackson, 1960) three times to completely remove iron oxides. We used the resulting residues as our natural matrix materials. The dithionite method extracts iron oxide/oxyhydroxide phases of iron (mainly hematite, goethite, with minor lepidocrocite, ferrihydrite, magnetite and maghemite) while leaving other minerals largely unaffected (Raiswell et al., 1994). After CBD-treatment, samples lost their brown color and became greenish (Fig. 4B). The removal of hematite and goethite is also shown by the loss of their corresponding peaks in the first derivative curve (Fig. 4B). Extracted Fe^{2+} concentrations in the CBD solution were measured on a UV-2100 spectrophotometer (UNICO Inc., Shanghai) to calculate the percent of CBD-extractable iron oxides in sediments. The iron oxide concentration ranges from 0.4 ∼ 1.3 wt.% in the calibration sample set. Based on the CBD-extractable iron data, first derivative curve comparison of samples with natural and synthetic iron oxides (not shown here), and

experience from previous studies (Harris and Mix, 1999; Ji et al., 2002), we estimate that in most samples hematite content ranges from 0.05 wt.% to 0.25 wt.%, with goethite content of 0.4 ∼ 1 wt.%.

(3) Adding Fe oxides to sample. Known quantities of pigment-grade synthetic hematite and goethite were added into the 14 samples following Scheinost et al. (1998). For hematite we used Pfizer R1559, pure red Fe oxide and for goethite we used Hoover Color Corp. Synox HY610 Yellow (Fig. 3). Both oxides were examined by XRD and have the appropriate crystallography, that is, they are fine-grained, i.e. micron or sub-micro powders, similar to the Fe oxide found in sediments (Ji et al., 2002). After the addition of the pigment-grade iron oxides the samples became brownish again and the hematite and goethite peaks returned in the first derivative graphs (Fig. 4C).

The fourteen calibration samples were prepared and analyzed with the spectrophotometer. Spectral violet, blue, green, yellow, orange, red and brightness (Fig. 2) were used as independent variables to be related to
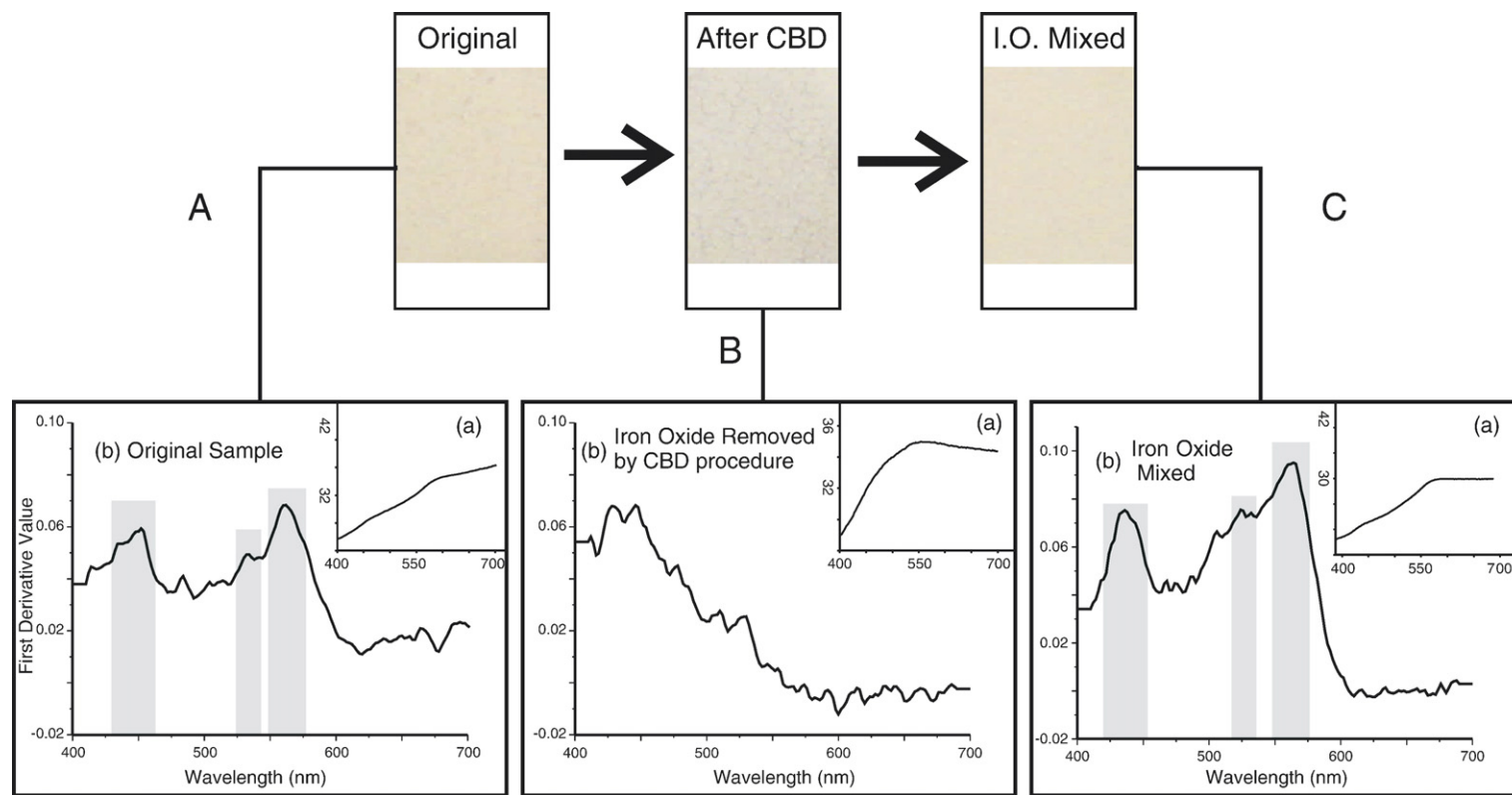
Fig. 4. Schematic of calibration sample preparation and measurement taking a typical sample (184/1143A/3H/2/125-126, mcd 16.25) as an example. (A) original sample, (B) sample after CBD-treatment, (C) iron oxide-free sample mixed with 0.2 wt.% hematite and 0.6 wt.% goethite. For each step the upper figure shows digital photo of microslides prepared for DRS measurement. The lower plots show the corresponding results. Raw reflectance curves are labeled with (a), while first derivative curves are labeled with (b). Peaks diagnostic for the presence of hematite and goethite are denoted with gray box. See text for details. (For interpretation of the references to color in this figure legend, the reader is referred to the web version of this article.)

Table 1
Hematite, goethite concentrations, reflectance in color bands and total reflectance (brightness) of the calibration sample set

Sample ID (leg/site-hole/core/section/interval)	Depth (mcd)	Violet (%)	Blue (%)	Green (%)	Yellow (%)	Orange (%)	Red (%)	Brightness	Hematite (wt. %)	Goethite (wt. %)
184/1143A/2H/4/5–6	7.87	13.62	11.60	22.79	11.00	14.97	26.03	7322	0.15	0.5
184/1143A/2H/4/45–46	8.27	14.00	12.02	23.33	10.83	14.55	25.27	7718	0.1	0.4
184/1143A/2H/5/15–16	9.47	13.60	11.73	23.38	10.96	14.68	25.64	7002	0.05	0.7
184/1143A/2H/5/25–26	9.57	12.88	11.35	23.22	11.16	15.03	26.36	6274	0.1	0.9
184/1143A/2H/5/65–66	9.97	12.48	10.87	22.41	11.32	15.56	27.35	6473	0.2	1
184/1143A/2H/6/25–26	11.07	13.47	11.41	22.63	11.05	15.08	26.36	6609	0.2	0.8
184/1143A/3H/1/115–116	14.65	13.98	11.81	22.79	10.89	14.81	25.73	6747	0.25	0.4
184/1143A/3H/2/125–126	16.25	15.50	12.96	23.79	10.31	13.67	23.76	5081	0	0
184/1143A/3H/2/135–136	16.35	13.92	11.88	23.25	10.83	14.58	25.55	6276	0.1	0.7
184/1143A/3H/2/145–146	16.45	13.90	11.85	23.17	10.84	14.62	25.62	6681	0.1	0.6
184/1143A/3H/3/135–136	17.85	13.85	11.93	23.47	10.90	14.56	25.29	6439	0.05	0.65
184/1143A/3H/5/25–26	19.75	14.19	11.95	22.98	10.85	14.66	25.37	6781	0.2	0.4
184/1143A/3H/6/15–16	21.15	14.71	12.40	23.60	10.57	14.09	24.63	7129	0	0.4
184/1143A/3H/7/5–6	22.55	13.88	11.99	23.38	10.86	14.57	25.33	6855	0.1	0.5

hematite and goethite concentration through multiple linear regression (Table 1). The choice of variables to include in the calibration equation was produced by a step-wise regression. For hematite, all variables except spectral green were excluded; and for goethite, only violet is used. The transfer functions we derived are:

$$\text{Hematite\%} = 4.26583 - 0.17929 * \text{Green\%} \quad (1)$$

$$\text{Goethite\%} = 5.10842 - 0.32771 * \text{Violet} \quad (2)$$

The correlation coefficients of these formulas are 0.905 for hematite and 0.928 for goethite. The estimated hematite and goethite content are plotted against the actual iron oxide concentration mixed into the samples (Fig. 5).

For hematite estimation, the R^2 is 0.82 with the root mean square of error (RMSE) of 0.0319 where hematite ranges from 0 to 0.25 wt.%. For goethite estimation R^2 and RMSE are 0.86 and 0.0938, respectively, where goethite ranges from 0 to 1 wt.% (Fig. 5). Thus, the calibration equations are satisfactory and small misfits may be attributed to errors introduced by changing matrix and by mixing the iron oxides. In general, the transfer function is robust enough to provide reliable estimates of hematite and goethite in ODP 1143 sediments.

5. Establishing the precipitation proxy

Since 1970s soil scientists have appreciated the climatic significance of iron oxide minerals derived
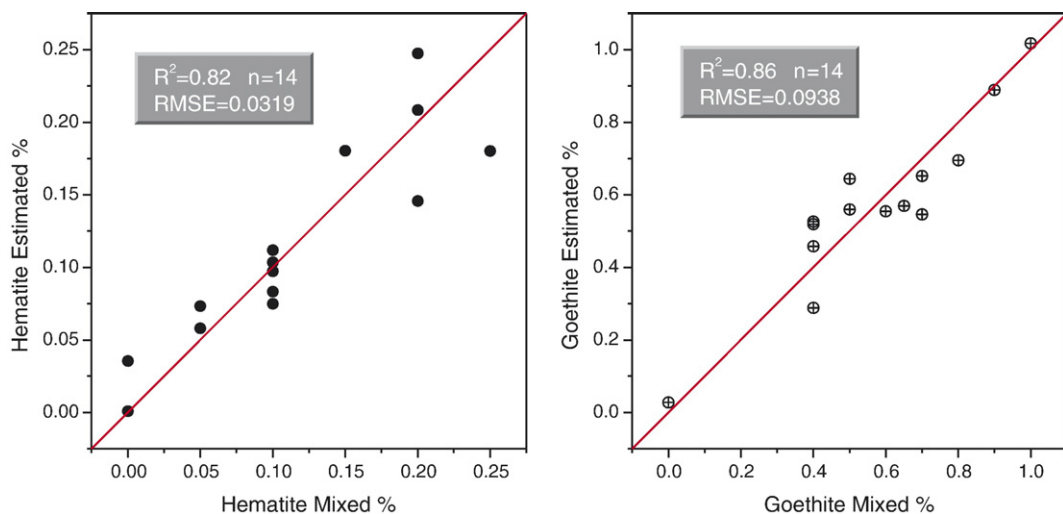

Fig. 5. Comparison of actual iron oxide content in the prepared samples with that predicted by the transfer function. Also shown are the 1:1 regression line, square of correlation coefficient (R^2), and the root mean square of error (RMSE).

from silicate weathering (Schwertmann, 1971). Hematite, derived from ferrihydrite through a dehydration–rearrangement process, is favored by warm and dry conditions; whereas goethite, forms directly from a variety of Fe source via solution, is favored by moist conditions. The formation processes for these two minerals are considered competitive, hence the rate of formation and the ratio of hematite to goethite are considered a climatic indicator (Kampf and Schwertmann, 1983; Schwertmann, 1988). Consequently, these two minerals, from a variety of sediments, have been used as proxies for climate change. For instance, Harris and Mix used diffuse reflectance spectra to derive goethite/(gotthite+hematite) ratio to monitor Pleistocene Amazon Basin precipitation variability (Harris and Mix, 1999) and the long-term continental erosion since late Miocene (Harris and Mix, 2002). This approach has been recently cited in a summary paper on climate-erosion connections (Molnar, 2004).

However, to use the Hm/Gt as a proxy for precipitation variations, we need to understand the process and environment of formation, transportation and deposition of the Fe oxides. We find ODP 1143 is located in the ideal place to record SE Asia precipitation for the following reasons:

(1) The Mekong Basin, where the majority of Fe oxides in ODP 1143 formed, has very high annual precipitation ($\sim$3000 mm/year) and temperature ($\sim$27 °C) thereby allowing weathering rates to reach $\sim$150 kg/ha/year (Oliva et al., 2003). Given an average soil density of <2.78 g/cm^3, the weathering rate is >5.4 cm/year. This means rapid formation of weathering minerals in response to a changing climate (Liu et al., 2004). These weathering products are moved rapidly to the SCS by the Mekong River, as indicated by the high ratio of Fe_{HR} (highly reactive iron oxide that is soluble in dithionite, mainly goethite and hematite) to FeT (total iron, Fe in secondary minerals such as hematite and goethite plus Fe bounded in primary minerals such as hornblende). The Fe_{HR}/FeT of Mekong is 0.66 whereas for the Amazon River it is only 0.47 (Poulton and Raiswell, 2002). This ratio is positively associated with the runoff ratio, which is average river runoff per unit area/average precipitation per unit area (Poulton and Raiswell, 2002). Thus, it not only indicates a high chemical weathering state in Mekong Basin, but also a high discharge ability of the Mekong River. Consequently, *in situ* produced iron oxides that have been balanced with the climate in the Mekong

Basin are rapidly delivered to the SCS by the Mekong River, recording climate changes with few time lags.

(2) Chemical weathering and iron oxide formation are controlled by both precipitation and temperature. However, the tropical SE Asia is dominated by precipitation changes, while temperature remains relatively stable. Even during the glacial maximum, summer temperatures around SCS were as high as that during interglacials (Wang et al., 1999). Since 85–90% of annual rainfall arrives in summer monsoon (Gupta et al., 2002) and the summer temperature is relatively stable, precipitation, rather than temperature, controls chemical weathering and thereby the Hm/Gt ratio. Thus, the Hm/Gt is a good measure of precipitation variability.

(3) Iron oxide minerals deposited in marine sediments are often subject to pore-water reduction (e.g. Poulton et al., 2004). Two observations indicate Fe oxides in ODP 1143 are of terrigenous origin and they have not been modified by reduction and/or reoxidation. First, unlike ODP cores drilled in northern SCS, pyrite, which is an indicator of iron oxide reduction, is absent from 1143 (Wang et al., 2000). Second, if diagenetic iron accumulates at the base of present oxidized layer, reducible iron must continually migrate upward to keep pace with sedimentation, dissolving diagenetic layer deeper in the sediment. Even if removal of the diagenetic layer buried below the oxidized zone were slow, the iron oxide abundance would decrease downcore (Harris and Mix, 1999). In contrast to this prediction, our goethite record fluctuates downcore with a tendency toward slightly higher concentrations above $\sim$22.5 mcd. Therefore, the precipitation signal is well-preserved in our Hm/Gt record.

To further validate the Hm/Gt record from ODP 1143 as a reliable proxy of precipitation variability, we compared the Hm/Gt ratios from the upper part of the core to the speleothem calcite $\delta^{18}O$ record from the Hulu and Dongge caves (see location in Fig. 1) in South China (Wang et al., 2001; Yuan et al., 2004). The stalagmite in these caves preserves the oxygen isotopic composition of meteoric precipitation and their $\delta^{18}O$ variations has been interpreted as an indicator of the summer monsoon precipitation (Wang et al., 2001; Yuan et al., 2004). Although the two records differ significantly in time resolution ($\sim$2 kyr for ODP 1143 and several decades for stalagmites) and dating method (orbital tuning for ODP 1143 and ^{230}Th absolute dating for stalagmites),

precipitation variations in Mekong Basin and South China inferred from these two records are generally consistent for the last 170 kyr (Fig. 6). Before 90 ka, three major peaks in precipitation loosely correlate to peaks in Chinese summer monsoon (Fig. 6). The leads or lags in Hm/Gt record may be attributed to the dating method that differs from that for stalagmites. The general correlation between Hm/Gt and stalagmite δ^{18}O indicates that Hm/Gt is a reliable proxy of monsoonal precipitation. Note the peak around 150 ka in stalagmite chronology or 155 ka in ODP 1143 chronology (Fig. 6). The high monsoonal precipitation around 150–155 ka, a typical glacial stage according to marine oxygen isotope stratigraphy (marine isotope stage 6, Martinson et al., 1987), suggests that precipitation variability significantly differs from glacial–interglacial climate cycles.

6. SE Asia precipitation and evolution of El Niño

We compared the long-term precipitation history of SE Asia inferred from this study to the long-term evolution of El Niño-Southern Oscillation (ENSO) in tropical Pacific (Fig. 7). Today, tropical trade winds drive ocean currents westward, resulting in a thick, warm, mixed layer and deep thermocline in the western equatorial Pacific (WEP) and a thin, warm, mixed layer and shallow thermocline in eastern equatorial Pacific (EEP). The ventilated thermocline in EEP brings cold, nutrient-rich waters to the

surface, setting up east–west sea surface temperature (SST) and atmospheric pressure gradient. At present, mean annual SSTs are 23 °C in EEP and 29 °C in WEP, yielding a temperature difference of 6 °C (Levitus and Boyer, 1994). The SST and associated pressure gradient drives the strong east–west atmospheric circulation pattern, Walker Circulation. The magnitude of the zonal SST gradient is an excellent indicator of the strength of Walker Circulation. The disruption of the SST asymmetry and Walker Circulation gives rise to El Niño conditions (Lawrence et al., 2006; Wara et al., 2005). According to modern meteorological studies, prolonged droughts in SE Asia are often associated with El Niño whereas severe floods tend to be associated with La Niña (e.g. Juneng and Tangang, 2005 and references therein). Changes in equatorial Pacific SST and ENSO in the geological past may also have had large consequences for tropical and extratropical climate (Molnar and Cane, 2002; Yin and Battisti, 2001).

We found a strong correlation between Asian monsoon precipitation recorded in ODP 1143 sediments and the development of paleo-El Niño conditions in the tropical Pacific as interpreted from Pacific deep-sea sediments (de Garidel-Thoron et al., 2005; Lawrence et al., 2006; Wara et al., 2005). Based on the Magnesium-to-Calcium ratio (Mg/Ca, Wara et al., 2005) or the alkenone unsaturation ratio paleothermometry (Lawrence et al., 2006), researchers were able to reconstruct SSTs in the EEP and WEP for
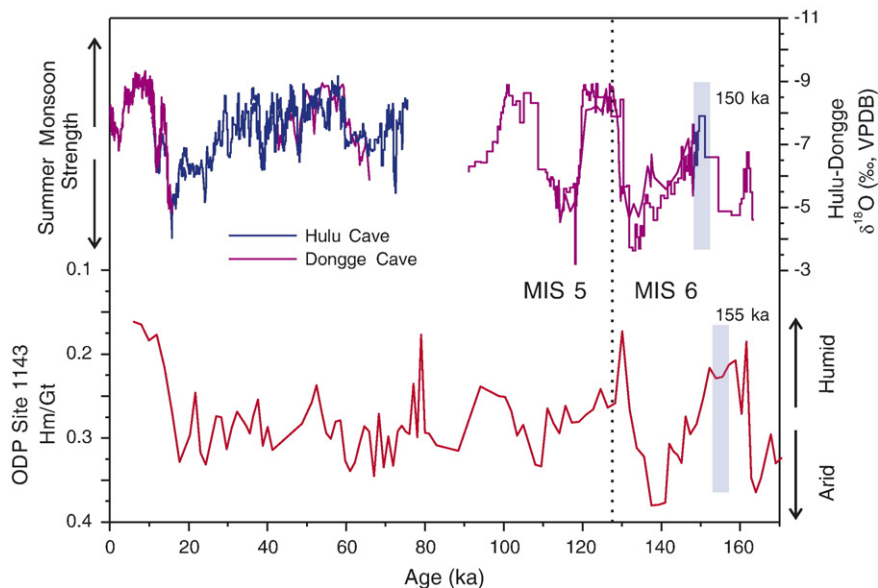

Fig. 6. Comparison of Hm/Gt from ODP 1143 and stalagmite oxygen isotopes from Hulu and Dongge Cave in south China (see location in Fig. 1) for the last 170 kyr. Note that the time resolution and chronology are different in the two records. High monsoonal precipitation intervals around 150 ka in stalagmite chronology or 155 ka in ODP 1143 chronology are highlighted by blue bars. Dashed line (128 ka) separated marine isotope stage (MIS) 5 and 6.
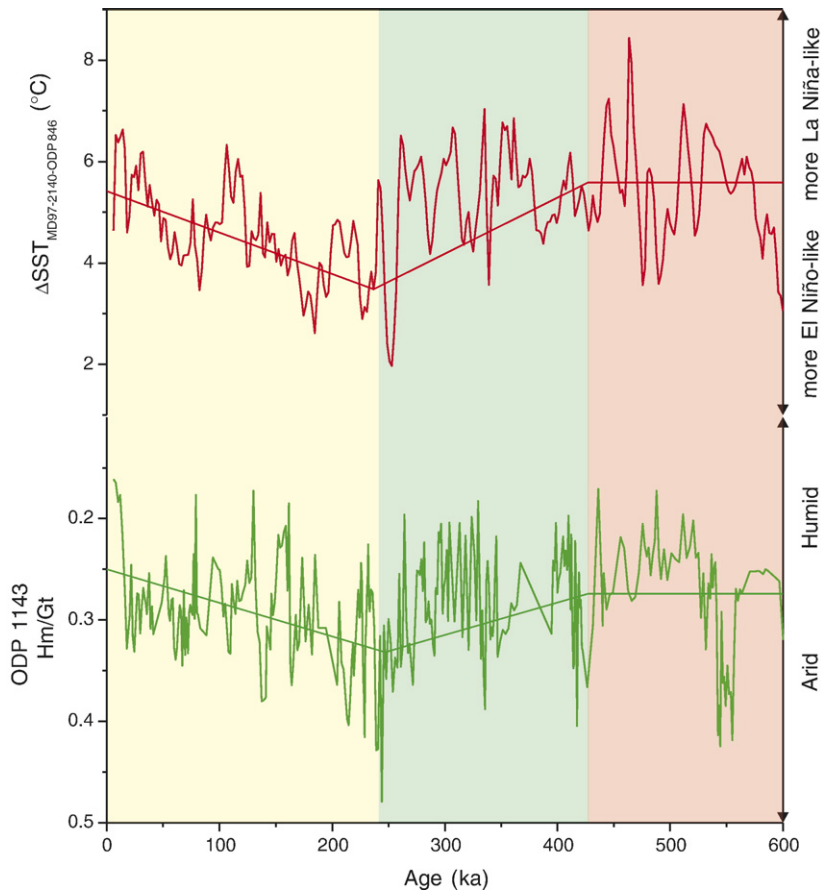
Fig. 7. Comparison of the sea surface temperature (SST) differences between western equatorial Pacific (WEP) and eastern equatorial Pacific (EEP) and Hm/Gt of ODP Site 1143 for the last 600 kyr. ΔSST were the differences between SST from core MD97-2140 of WEP (de Garidel-Thoron et al., 2005) and SST from core ODP 846 of EEP (Liu and Herbert, 2004). Both SST records were interpolated from 600 to 0 ka with an increment of 2 kyr before ΔSST calculation. Higher ΔSST indicate a more La Niña-like condition whereas lower ΔSST are indicative of El Niño climate. ΔSST and Hm/Gt evolutions are subdivided into three time intervals shaded with different colors. The straight lines represent the long-term trend of the records.

the last five million years. During this time, the SST in WEP is relatively stable, while EEP temperatures decreased and the rate of decrease has accelerated since late Pliocene (~2.2 Ma). This phenomenon is attributed to the ending of permanent El Niño conditions in the tropical Pacific during Pliocene (Fedorov et al., 2006; Wara et al., 2005). We calculated the ΔSST, the differential SST between the WEP and EEP. The SST of EEP is taken from ODP 848 and is based on alkenone reconstruction (Liu and Herbert, 2004), whereas the SST of WEP record is based on Mg/Ca paleothermometry of Hole MD97-2140 (de Garidel-Thoron et al., 2005). Both records were interpolated before the ΔSST is calculated.

Fig. 7 shows that the evolution of both El Niño and monsoonal precipitation for the last 600 ka can be subdivided into three periods: from 600–430 ka the equatorial Pacific was dominated by La Niña-like patterns and precipitation in SE Asia was high; from

430–240 ka the tropical Pacific was characterized by the development of an El Niño climate and precipitation decreased continuously; from ~240 ka to the present precipitation begins to increase as La Niña climates became more common. From our analysis it appears that for the last 600 kyr, Asian monsoon precipitation has co-evolved with ENSO of equatorial Pacific, revealing that the equatorial Pacific may play a remarkable role in controlling SE Asia precipitation. This evolutionary trend of Asian monsoon precipitation since 600 ka is not reflected in benthic $\delta^{18}O$ from the same core (Tian et al., 2002). The cause of such changes of El Niño climate in equatorial Pacific remains to be explored.

7. Discussion

The high-resolution reconstruction of Asian monsoon precipitation variability displayed in the Hm/Gt ratio

enables us to discuss orbital-scale variations, as well as long-term trends of the Pleistocene Asian monsoon.

7.1. Orbital-scale monsoon changes

The driving force for Asian monsoon changes over an orbital scale is still an open question. Early works of Kutzbach proposed that the Northern Hemisphere (NH) summer insolation drives the tropical monsoon (Kutzbach, 1981) and this point of view was supported by Ruddiman, (2006). However, Clemens and Prell suggested a more sophisticated forcing mechanism tied to latent heat transport from the Southern Hemisphere and global ice volume (Clemens and Prell, 2003). The apparent inconsistency in the monsoon forcing results in different periodicity and phasing of the Asian monsoon variations as presumed by those researchers. According to Ruddiman, the monsoon should respond to the precession-dominated NH summer insolation with near-zero phases (Ruddiman, 2006). This idea is supported by the stalagmites from south China (Wang et al., 2001; Yuan et al., 2004). Ruddiman also claimed that the monsoon indices from marine sediments used by Clemens and Prell may not be tightly coupled to the summer monsoon since proxies reconstructed from deep-sea sediments are often "contaminated" by other processes such as the winter monsoon and ice volume (Ruddiman, 2006). However, after the re-examination of the Hulu–Dongge Cave stalagmite $\delta^{18}O$, Clemens and Prell indicated that their interpretation is consistent with marine proxies and they both have significant phase lags on the precession and obliquity band. They also cited recent climate model experiments to support the complicated monsoon forcing involving feedbacks from the Southern Hemisphere (Clemens and Prell, 2007).

Since the chronology of ODP 1143 was established by tuning the benthic $\delta^{18}O$ to Earth's orbit with a presumed phase lag (Tian et al., 2002), we find it may be problematic to discuss the phase and/or periodicity issues of the Hm/Gt record. However, if the summer monsoon proxies reconstructed from marine sediments are often influenced by other factors as asserted by Ruddiman (2006), the general consistency of our Hm/Gt record and the stalagmite record indicates that Hm/Gt is a good summer monsoon proxy that overcomes those drawbacks. Furthermore, the marine sediment derived Hm/Gt record and the Hulu–Dongge Cave record revealed significant differences between summer monsoon and the glacial–interglacial climate cycles. We argue that the previously presumed summer monsoon intensification during interglacial stages and weakening during glacial stages may be invalid. Our data docu-

ments that low-latitude hydrological/atmospheric circulation is a relatively independent component of climate that differs from the global temperature cycle. This conclusion may have profound implications for monsoon regions' ecology, hydrology, and even the Global biogeochemical cycling of key elements.

7.2. Long-term monsoon trends

The reconstructed Asian monsoon precipitation variability from the Hm/Gt record can be subdivided into three periods (Fig. 7). Although there is no other continuous precipitation record spanning this 600–0 ka interval we find some isolated precipitation events that can be compared to our Hm/Gt record. According to the Hm/Gt record, drought occurred around 240 ka. During 280 ~ 140 ka, a major central-western Italy stalagmite growth hiatus was found (Drysdale et al., 2004), coinciding with the lowest precipitation intervals as reflected by Hm/Gt. Freezing conditions during glacial maximum (Drysdale et al., 2004) cannot explain the long-lasting growth terminations experiencing both glacial (MIS 6) and interglacial stages (MIS 7). We argue that the reduced precipitation during this time may stop the stalagmite growth. 600–430 ka was characterized by high precipitation with a maximum around 520 ka (Fig. 7). In the equatorial Indian Ocean, an exceptional $\delta^{18}O$ depletion peak at ~525 ka in Core MD90-0963 was interpreted by Bassinot et al. (1994b) as a large freshwater discharge to the Ocean. This coincides with a thick sapropel layer in the eastern Mediterranean that indicates high rainfall (Rossignol-Strick et al., 1998), and a well-developed paleosol unit S5 on the Loess Plateau of China (Liu, 1985). This precipitation peak was linked to a marine carbon isotope maximum event $\delta^{13}Cmax-II$ in the ~500 kyr "super cycle" of marine foraminiferal $\delta^{13}C$ (Wang et al., 2003, 2004). A number of hypotheses were proposed to explain the low-latitude monsoon precipitation in controlling the Global carbon cycle (Wang et al., 2003, 2004). To these we add that the continuous increase in precipitation from 240 ka to present may have induced the $\delta^{13}Cmax-I$ event at 60 ~ 0 ka.

Fig. 7 shows that SE Asia precipitation may have co-evolved with El Niño since 600 ka. We suggest that equatorial Pacific oceanic–atmospheric dynamics might be the main controlling factor of long-term precipitation trends in SE Asia. Modern meteorological studies link the Asian monsoon to the two off-equatorial anticyclones during El Niño episodes, one over the south Indian Ocean and one over the western North Pacific. The establishment of these anomalous anticyclones would result in notable anomalies, such as outgoing long wavelength radiation,

SST, evaporation, and moisture transport by the Asian monsoon in SE Asia (Juneng and Tangang, 2005). Although we cannot expect a perfect reproduction of this scenario during the geologic past, the extrapolation of these "El Niño — drought, La Niña — humid" associations (Molnar and Cane, 2002) in SE Asia are very likely for the last 600 kyr as evidenced by our ODP 1143 Hm/Gt record.

8. Conclusions

In this study we utilized a procedure for measuring the concentrations of hematite and goethite, two climatic significant Fe oxide minerals, with diffuse reflectance spectroscopy and extended its application to marine sediments. The Hm/Gt ratios in ODP 1143 sediments correlate well with variations of stalagmite oxygen isotopes in south China, suggesting that the Hm/Gt record from ODP 1143 sediments provides a unique, long-term record of Asian monsoon precipitation in SE Asia over the last 600,000 years. On an orbital time scale, the Hm/Gt and stalagmite $\delta^{18}O$ monsoon records highlight the relative independence of the low-latitude atmospheric/hydrologic cycle from the glacial–interglacial temperature cycle. For the last 600 ka, the Asian monsoon also displayed significant trends in evolution that may be regulated by the El Niño/La Niña conditions in equatorial Pacific. The trends evolution brought flood or drought to monsoon regions, and may affect the global biogeochemical cycling of key elements such as carbon.

Acknowledgements

Appendix A. Supplementary data

Supplementary data associated with this article can be found, in the online version, at doi:10.1016/j.epsl.2007.09.022.

References

Balsam, W.L., Deaton, B.C., 1991. Sediment dispersal in the Atlantic Ocean: evaluation by visible light spectra. Rev.Aquat. Sci. 4, 411–447.

Balsam, W.L., Deaton, B.C., Damuth, J.E., 1998. The effects of water content on diffuse reflectance spectrophotometry studies of deep-sea sediment cores. Mar. Geol. 149, 177–189.

Balsam, W.L., Deaton, B.C., Damuth, J.E., 1999. Evaluating optical lightness as a proxy for carbonate content in marine sediment cores. Mar. Geol. 161, 141–153.

Balsam, W., Ji, J.F., Chen, J., 2004. Climatic interpretation of the Luochuan and Lingtai loess sections, China, based on changing iron oxide mineralogy and magnetic susceptibility. Earth Planet. Sci. Lett. 223, 335–348.

Bassinot, F., Beaufort, L., Vincent, E., Labeyrie, L., Rostek, F., Muller, P.J., Quidelleur, X., Lancelot, Y., 1994a. Coarse fraction fluctuations in pelagic carbonate sediments from the tropical Indian Ocean: a 1500-kyr record of carbonate dissolution. Paleoceanography 9, 579–600.

Bassinot, F., Labeyrie, L., Vincent, E., Quidelleur, X., Shackleton, N.J., Lancelot, Y., 1994b. The astronomical theory of climate and the age of the Brunhes–Matuyama magnetic reversal. Earth Planet. Sci. Lett. 126, 91–108.

Cheng, H., Edwards, R.L., Wan, Y.J., Kong, X.G., Ming, Y.F., Kelly, M.J., Wang, X.F., Gallup, C.D., Liu, W.G., 2006. A penultimate glacial monsoon record from Hulu Cave and two-phase glacial terminations. Geology 34, 217–220.

Clark, R.N., Roush, T.L., 1984. Reflectance spectroscopy: Quantitative analysis techniques for remote sensing application. J. Geophys. Res. 89, 6329–6340.

Clemens, S.C., Prell, W.L., 2003. A 350,000 year summer-monsoon multi-proxy stack from the Owen ridge, Northern Arabian sea. Mar. Geol. 201, 35–51.

Clemens, S.C., Prell, W.L., 2007. The timing of orbital-scale Indian monsoon changes. Quat. Sci. Rev. 26, 275–278.

Clift, P.D., 2006. Controls on the erosion of Cenozoic Asia and the flux of clastic sediment to the ocean. Earth Planet. Sci. Lett. 241, 571–580.

Deaton, B.C., Balsam, W.L., 1991. Visible spectroscopy — a rapid method for determining hematite and goethite concentration in geological materials. J. Sediment. Petrol. 61, 628–632.

Debret, M., Desmet, M., Balsam, W., Copard, Y., Francus, P., Laj, C., 2006. Spectrophotometer analysis of Holocene sediments from an anoxic fjord: Saanich Inlet, British Columbia, Canada. Mar. Geol. 229, 15–28.

de Garidel-Thoron, T., Rosentral, Y., Bassinot, F., Beaufort, L., 2005. Stable see surface temperatures in the western Pacific warm pool over the past 1.75 million years. Nature 433, 294–298.

Drysdale, R.N., Zanchetta, G., Hellstrom, J.C., Fallick, A.E., Zhao, J.X., Isola, I., Bruschi, G., 2004. Palaeoclimatic implications of the growth history and stable isotope (delta O-18 and delta C-13) geochemistry of a Middle to Late Pleistocene stalagmite from central-western Italy. Earth Planet. Sci. Lett. 227, 215–229.

Edwards, R.L., Chen, J.H., Ku, T.-L., Wasserburg, G.J., 1987. Precise timing of the Last Interglacial period from Mass Spectrometric determination of thorium-230 in corals. Science 236, 1547–1553.

Fedorov, A.V., Dekens, P.S., McCarthy, M., Ravelo, A.C., deMenocal, P.B., Barreiro, M., Pacanowski, R.C., Philander, S.G., 2006. The Pliocene paradox (mechanisms for a permanent El Niño). Science 312, 1485–1489.

Gupta, A., Hock, L., Huang, X., Chen, P., 2002. Evaluation of part of the Mekong River using satellite imagery. Geomorphology 44, 221–239.

Harris, S.E., Mix, A.C., 1999. Pleistocene precipitation balance in the Amazon Basin recorded in deep sea sediments. Quat. Res. 51, 14–26.

Harris, S.E., Mix, A.C., 2002. Climate and tectonic influences on continental erosion of tropical South America, 0–13 Ma. Geology 30, 447–450.

Hunt, G.R., Salisbury, J.W., 1970. Visible and near-infrared spectra of minerals and rocks, I. Silicate minerals. Mod. Geol. 1, 283–300.

Ji, J.F., Balsam, W., Chen, J., Liu, L.W., 2002. Rapid and quantitative measurement of hematite and goethite in the Chinese loess-paleosol sequence by diffuse reflectance spectroscopy. Clays Clay Miner. 50, 208–216.

Ji, J.F., Chen, J., Balsam, W., Lu, H.Y., Sun, Y.B., Xu, H.F., 2004. High resolution hematite/goethite records from Chinese loess sequences for the last glacial–interglacial cycle: rapid climatic response of the East Asian Monsoon to the tropical Pacific. Geophys. Res. Lett. 31. doi:10.1029/2003GL018975.

Judd, D.B., Wyszecki, G., 1975. Color in Business, Science, and Industry. John Wiley and Sons, New York. 553 pp.

Juneng, L., Tangang, F.T., 2005. Evolution of the ENSO-related rainfall anomalies in Southeast Asia region and its relationship with atmosphere–ocean variations in Indo-Pacific sector. Clim. Dyn. 25, 337–350.

Kampf, N., Schwertmann, U., 1983. Goethite and hematite in a climo-sequence in southern Brazil and their application in classification of kaolinitic soils. Geoderma 29, 27–39.

Kutzbach, J.E., 1981. Monsoon climate of the early Holocene: climate experiment with the Earth's orbital parameters for 9000 years ago. Science 214, 59–61.

Lawrence, K.T., Liu, Z.H., Herbert, T.D., 2006. Evolution of the Eastern Tropical Pacific through Plio-Pleistocene Glaciation. Science 312, 79–83.

Levitus, S. and Boyer, T.P., 1994, World Ocean Atlas: Washington, DC, NOAA Atlas NESDros. Inf. Serv.

Liu, T.S., 1985. Loess and the Environment. China Ocean Press, Beijing.

Liu, Z., Herbert, T.D., 2004. High-latitude influence on the eastern equatorial Pacific climate in the early Pleistocene epoch. Nature 427, 720–723.

Liu, Z.F., Colin, C., Trentesaux, A., Blamart, D., Bassinot, F., Siani, G., Sicre, M.A., 2004. Erosional history of the eastern Tibetan Plateau since 190 kyr ago: clay mineralogical and geochemical investigations from the southwestern South China Sea. Mar. Geol. 209, 1–18.

Liu, Z.F., Colin, C., Trentesaux, A., Siani, G., Frank, N., Blamart, D., Farid, S., 2005. Late Quaternary climatic control on erosion and weathering in the eastern Tibetan Plateau and the Mekong Basin. Quat. Res. 63, 316–328.

Martinson, D.G., Pisias, N.G., Hays, J.D., Imbrie, J., Moore, T.C., Shackleton, N.J., 1987. Age dating and the orbital theory of the ice ages: development of a high-resolution 0 to 300,000-year chronostratigraphy. Quat. Res. 27, 1–29.

Mehra, O.P., Jackson, M.L., 1960. Iron oxide removal from soils and clays by a dithionate-citrate system buffered with sodium bicarbonate. Clays Clay Miner. 7, 317–327.

Molnar, P., 2004. Late cenozoic increase in accumulation rates of terrestrial sediment: How might climate change have affected erosion rates? Ann. Rev. Earth Planet. Sci. 32, 67–89.

Molnar, P., Cane, M.A., 2002. El Nino's tropical climate and teleconnections as a blueprint for pre-Ice Age climates. Paleocea-nography 17. doi:10.1029/2001PA000663.

Oliva, P., Viers, J., Dupre, B., 2003. Chemical weathering in genetic environments. Chem. Geol. 202, 225–256.

Poulton, S.W., Canfield, D.E., 2005. Development of a sequential extraction procedure for iron: implications for iron partitioning in continentally derived particulates. Chem. Geol. 214, 209–221.

Poulton, S.W., Raiswell, R., 2002. The low-temperature geochemical cycle of iron: From continental fluxes to marine sediment deposition. Am. J. Sci. 302, 774–805.

Poulton, S.W., Krom, M.D., Raiswell, R., 2004. A revised scheme for the reactivity of iron (oxyhydr)oxide minerals towards dissolved sulfide. Geochim. Cosmochim. Acta 68, 3703–3715.

Raiswell, R., Canfield, D.E., Berner, R.A., 1994. A comparison of iron extraction methods for the determination of degree of pyritisation and the recognition of iron-limited pyrite formation. Chem. Geol. 111, 101–110.

Rossignol-Strick, M., Paterne, M., Bassinot, F.C., Emeis, K.C., De Lange, G.J., 1998. An unusual mid-Pleistocene monsoon period over Africa and Asia. Nature 392, 269–272.

Ruddiman, W.F., 2006. What is the timing of orbital-scale monsoon changes? Quat. Sci. Rev. 25, 657–658.

Scheinost, A.C., Chavernas, A., Barron, V., Torrent, J., 1998. Use and limitations of second-derivative diffuse reflectance spectroscopy in the visible to near-infrared range to identify and quantify Fe oxide minerals in soils. Clays Clay Miner. 46, 528–536.

Schwertmann, U., 1971. Transformation of hematite to goethite in soils. Nature 232, 624–625.

Schwertmann, U., 1988. Occurrence and formation of iron oxides in various pedoenvironments. In: Stucki, J.W. (Ed.), Iron in soils and clay minerals. D. Reidel, Norwell, pp. 267–308.

Schwertmann, U., Murad, E., 1983. Effect of pH on the formation of goethite and hematite from ferrihydrite. Clays Clay Miner. 31, 277–284.

Shen, C.C., Lee, T., Liu, K.K., Hsu, H.H., Edwards, R.L., Wang, C.H., Lee, M.Y., Chen, Y.G., Lee, H.J., Sun, H.T., 2005. An evaluation of quantitative reconstruction of past precipitation records using coral skeletal Sr/Ca and delta O-18 data. Earth Planet. Sci. Lett. 237, 370–386.

Tamburini, F., Adatte, T., Follmi, K., Bernasconi, S.M., Steinmann, P., 2003. Investigating the history of East Asian monsoon and climate during the last glacial–interglacial period (0–140 000 years): mineralogy and geochemistry of ODP Sites 1143 and 1144, South China Sea. Mar. Geol. 201, 147–168.

Tian, J., Wang, P.X., Cheng, X.R., Li, Q.Y., 2002. Astronomically tuned Plio-Pleistocene benthic delta O-18 record from South China Sea and Atlantic–Pacific comparison. Earth Planet. Sci. Lett. 203, 1015–1029.

Trentesaux, A., Liu, Z., Colin, C., Boulay, S., Wang, P.X., 2003. Data report: Pleistocene paleoclimatic cyclicity of southern China: clay mineral evidence recorded in the South China Sea (ODP Site 1146). In: Prell, W., Wang, P.X., Blum, P., Rea, D.K., Clemens, S. (Eds.), Proc. ODP, Sci. Results, vol. 184. Ocean Drilling Program, College Station, TX, pp. 1–10.

Wan, S.M., Li, A., C., Clift, P.D., Jiang, H.Y., 2006. Development of the East Asian summer monsoon: evidence from the sediment record in the South China Sea since 8.5 Ma. Palaeogeogr. Palaeoclimatol. Palaeoecol. 241, 139–159.

Wang, P.X., Wang, L., Bian, Y.H., Jian, Z.M., 1995. Late Quaternary paleoceanography of the South China Sea: surface circulation and carbonate cycles. Mar. Geol. 127, 145–165.

Wang, L., Sarnthein, M., Erlenkeuser, H., Grimalt, J.O., Grootes, P., Heilig, S., Ivanova, E., Kienast, M., Pelejero, C., Pflaumann, U., 1999. East Asian monsoon climate during the Late Pleistocene: high-resolution sediment records from the south China Sea. Mar. Geol. 156, 245–284.

Wang, P.X., Prell, W., Blum, P., Rea, D.K., Clemens, S., 2000. Proceedings of the Ocean Drilling Program. Initial Rep., vol. 184. Ocean Drilling Program, College Station, Texas.

Wang, Y.J., Cheng, H., Edwards, R.L., An, Z.S., Wu, J.Y., Shen, C.C., Dorale, J.A., 2001. A high-resolution absolute-dated Late Pleistocene monsoon record from Hulu Cave, China. Science 294, 2345–2348.

Wang, P.X., Tian, J., Cheng, X.R., Liu, C.L., Xu, J., 2003. Carbon reservoir changes preceded major ice-sheet expansion at the mid-Brunhes event. Geology 31, 239–242.

Wang, P.X., Tian, J., Cheng, X.R., Liu, C.L., Xu, J., 2004. Major Pleistocene stages in a carbon perspective: The South China Sea record and its global comparison. Paleoceanography 19. doi:10.1029/2003PA000991.

Wang, P.X., Clemens, S., Beaufort, L., Braconnot, P., Ganssen, G., Jian, Z.M., Kershaw, P., Sarnthein, M., 2005. Evolution and variability of the Asian monsoon system: state of the art and outstanding issues. Quat. Sci. Rev. 24, 595–629.

Wara, M.W., Ravelo, A.C., Delaney, M.L., 2005. Permanent El Nino-like conditions during the Pliocene warm period. Science 309, 758–761.

Webster, P.J., 1994. The role of hydrological processes in ocean–atmosphere interactions. Rev. Geophys. 32, 427–476.

Wehausen, R., Tian, J., Brumsack, H.J., Cheng, X.R., Wang, P.X., 2003. Geochemistry of Pliocene sediments from ODP site 1143 (Southern South China Sea). In: Prell, W.L., Wang, P.X., Blum, P., Rea, D.K., Clemens, S. (Eds.), Proc. ODP, Sci. Results, vol. 184. Ocean Drilling Program, Colledge Station, TX, pp. 1–25.

Wei, G.J., Liu, Y., Li, X.H., Chen, M.H., Wei, W.C., 2003. High-resolution elemental records from the South China See and their paleoproductivity implications. Paleoceanography 18. doi:10.1029/2002PA000826.

Yin, J.H., Battisti, D.S., 2001. The importance of tropical sea surface temperature patterns in simulations of last glacial maximum climate. J. Climate 14, 565–581.

Yuan, D.X., Cheng, H., Edwards, R.L., Dykoski, C.A., Kelly, M.J., Zhang, M.L., Qing, J.M., Lin, Y.S., Wang, Y.J., Wu, J.Y., Dorale, J.A., An, Z.S., Cai, Y.J., 2004. Timing, duration, and transitions of the Last Interglacial Asian Monsoon. Science 304, 575–578.